The Astrophysical Journal, 991:109 (10pp), 2025 September 20 https://doi.org/10.3847/1538-4357/adf29e

Exploring the Masses of the Two Most Distant Gravitational Lensing Clusters at Cosmic Noon

Jinhyub Kim[1], M. James Jee[2,3], Stefano Andreon[4], Tony Mroczkowski[5], Lance Miller[1], Joshiwa van Marrewijk[5,6], and Hye Gyeong Khim[2]
[1] Department of Physics, University of Oxford, Denys Wilkinson Building, Keble Road, Oxford OX1 3RH, UK; jinhyub.kim@physics.ox.ac.uk
[2] Department of Astronomy, Yonsei University, 50 Yonsei-ro, Seoul 03722, Republic of Korea; mkjee@yonsei.ac.kr
[3] Department of Physics, University of California, Davis, One Shields Avenue, Davis, CA 95616, USA
[4] INAF-Osservatorio Astronomico di Brera, via Brera 28, 20121, Milano, Italy
[5] European Southern Observatory (ESO), Karl-Schwarzschild-Strasse 2, Garching 85748, Germany
[6] Leiden Observatory, Leiden University, P.O. Box 9513, 2300 RA Leiden, The Netherlands
Received 2024 December 18; revised 2025 July 20; accepted 2025 July 20; published 2025 September 19

Abstract

Observations over the past decade have shown that galaxy clusters undergo the most transformative changes during the $z = 1.5$–2 epoch. However, challenges such as low lensing efficiency, high shape measurement uncertainty, and a scarcity of background galaxies have prevented us from characterizing their masses with weak gravitational lensing (WL) beyond redshift $z \sim 1.75$. In this paper, we report the successful WL detection of JKCS 041 and XLSSC 122 at $z = 1.80$ and $z = 1.98$, respectively, utilizing deep infrared imaging data from the Hubble Space Telescope with careful removal of instrumental effects. These are the most distant clusters ever measured through WL. The mass peaks of JKCS 041 and XLSSC 122, which coincide with the X-ray peak positions of the respective clusters, are detected at the $\sim 3.7\sigma$ and $\sim 3.2\sigma$ levels, respectively. Assuming a single spherical Navarro–Frenk–White profile, we estimate that JKCS 041 has a virial mass of $M_{200c} = (5.4 \pm 1.6) \times 10^{14} M_{\odot}$, while the mass of XLSSC 122 is determined to be $M_{200c} = (3.3 \pm 1.8) \times 10^{14} M_{\odot}$. These WL masses are consistent with the estimates inferred from their X-ray observations. We conclude that although the probability of finding such massive clusters at their redshifts is certainly low, their masses can still be accommodated within the current ΛCDM paradigm.

Unified Astronomy Thesaurus concepts: Observational cosmology (1146); High-redshift galaxy clusters (2007); Galaxy clusters (584); Dark matter (353); Weak gravitational lensing (1797); Gravitational lensing (670)

1. Introduction

As the largest gravitationally bound objects detached from the Hubble flow, galaxy clusters form at the intersections of cosmic filaments, growing via the gravitational accretion of matter over cosmic time. They serve as powerful astrophysical laboratories where insights into plasma physics, galaxy evolution, and dark matter properties can be gained. In addition, their aggregate statistics are invaluable diagnostics of the growth rate of the large-scale structure of the Universe.

Cluster number densities per mass bin, referred to as the mass function, are sensitive to cosmological parameters, in particular, the matter density Ω_M and the normalization of the matter power spectrum σ_8 (e.g., S. Borgani & A. Kravtsov 2011; S. Planelles et al. 2015). However, since the effects of the two parameters Ω_M and σ_8 are highly degenerate, it is necessary to use a wide redshift baseline to break the degeneracy (e.g., N. A. Bahcall et al. 1997; N. A. Bahcall & X. Fan 1998; B. Sartoris et al. 2016). Consequently, increasing efforts have been made to find and measure galaxy clusters at higher and higher redshifts, driven by a range of scientific objectives, including constraining cosmological parameters and understanding cluster formation and evolution.

A number of campaigns have been conducted to find high-z clusters and to determine their masses through galaxy, X-ray, and Sunyaev–Zel'dovich (SZ) observations (e.g., R. Fassbender et al. 2011; N. Mehrtens et al. 2012; L. E. Bleem et al. 2015; M. Hilton et al. 2021). These surveys are efficient at detecting high-z clusters. However, mass estimation from these observables is prone to bias, as it assumes hydrostatic equilibrium or scaling relations that can vary with cluster redshift (e.g., K. Nelson et al. 2012; E. Rasia et al. 2014).

Weak gravitational lensing (WL) is a powerful tool to measure accurate cluster masses since the lensing signal does not depend on the dynamical state of the lens. Thus, many cosmological studies based on cluster mass function calibrate the mass using WL results. However, WL studies of high-redshift clusters are difficult in several aspects. First, high-redshift lenses ($z_{\rm lens} > 1$) are less effective than intermediate-redshift lenses. For instance, when the source is at $z_{\rm source} \sim 2$, the lensing efficiency peaks at $z_{\rm lens} \sim 0.5$. Beyond this point, the efficiency declines, making the lensing-induced distortion weaker at higher lens redshifts for a given lens mass. Second, the lensing signal comes from very distant, faint, and small galaxies, whose shapes are hard to determine precisely. Third, the source density decreases substantially because only the sources behind the already high-redshift cluster are lensed.

Space-based observations can overcome these challenges by providing higher-resolution images with smaller point-spread functions (PSFs) than ground-based observations, enabling us to measure subtle distortions in much fainter and smaller background galaxy images more reliably. In addition, significant advantages are gained when using infrared (IR) imaging data for high-redshift WL, as source galaxy shapes at

high redshifts ($z > 1$) are easier to characterize in IR than in optical; the surface brightness is higher, and the light profile is smoother. Indeed, most existing WL studies of high-z galaxy clusters at $z > 1$ relied on Hubble Space Telescope (HST) imaging data (e.g., M. J. Jee et al. 2011; T. Schrabback et al. 2018; J. Kim et al. 2019), and a substantial fraction of lenses at $z > 1.4$ have been measured with IR imaging data. Nevertheless, the number of clusters measured with WL rapidly drops with redshift. For instance, at $z > 1.7$, only three galaxy clusters have been probed by WL to date: SPT-CL J0459-4947 at $z = 1.71$ (SPT0459; H. Zohren et al. 2022), SpARCS1049+56 at $z = 1.71$ (SpARCS1049; K. Finner et al. 2020), and IDCS J1426+3508 at $z = 1.75$ (IDCS1426; M. J. Jee et al. 2017), with the latter IDCS1426+3508 at $z = 1.75$ currently being the highest-redshift lensing cluster on record.

Studies of high-z galaxy clusters at $z \gtrsim 1.5$ over the past decade have presented many remarkable findings on the cluster galaxies and their environments. While the $1.5 \lesssim z \lesssim 2$ epoch may be the most transformative (i.e., transition from proto-cluster to cluster) phase (e.g., R. A. Overzier 2016; T. Wang et al. 2016; Y.-K. Chiang et al. 2017) in cluster evolution for the average population, many observations (e.g., S. Andreon et al. 2014; A. B. Newman et al. 2014; E. Noordeh et al. 2021; S. Mei et al. 2023) indicate that in some high-redshift clusters, mature (early-type) galaxies dominate the cluster population, as they do at the present epoch. Additionally, contrary to the theoretical prediction, abundant intracluster light has been detected in this epoch (H. Joo & M. J. Jee 2023; S. V. Werner et al. 2023), with a fraction comparable to that found in their low-z counterparts. Also, X-ray observations show that some clusters in this epoch possess X-ray emitting intracluster medium, which is typically used as a criterion to distinguish protoclusters and clusters (e.g., R. A. Overzier 2016). However, conspicuously missing is our understanding of their dark matter potential well, which is one of the most critical environmental factors.

We present WL masses of JKCS 041 and XLSSC 122 at $z = 1.80$ and $z = 1.98$, respectively, based on HST Wide Field Camera 3 (WFC3)/IR imaging. They represent the most distant clusters measured with WL. JKCS 041 was discovered in 2006 from the J and K observations of the UKIRT Infrared Deep Sky Survey (A. Lawrence et al. 2007) Early Data Release (S. Dye et al. 2006) as a clustering of sources of similar colors (S. Andreon et al. 2009). S. Andreon et al. (2009) also revealed a diffuse X-ray emission with a temperature of $7.4^{+5.3}_{-3.3}$ keV from the Chandra observation. The MUSTANG-2 SZ observation found that the cluster has a low central pressure with the SZ peak $\sim 26''$ offset from the X-ray peak (S. Andreon et al. 2023). On the other hand, XLSSC 122 was originally detected as an extended X-ray source in the XMM Large Scale Structure survey (M. Pierre et al. 2004) and was later found to coincide with a compact overdensity of galaxies with $z_{\rm phot} = 1.9 \pm 0.2$ (J. P. Willis et al. 2013). From the HST G141 grism data, J. P. Willis et al. (2020) confirmed 37 member galaxies at a mean redshift of 1.98 and demonstrated that XLSSC 122 is indeed a surprisingly mature cluster with evolved members when the Universe was less than a quarter of its current age. Multi-wavelength studies indicate that both JKCS 041 and XLSSC 122 may be massive clusters ($\gtrsim 1.5 \times 10^{14}\, M_\odot$, S. Andreon et al. 2014; J. van Marrewijk et al. 2024) for their redshifts. However, their masses have yet to be confirmed through gravitational lensing, as its signal does not depend on their unknown dynamical states.

This paper is organized as follows. In Section 2, we describe our HST WFC3/IR imaging data, their reduction, and the WL analysis procedure. We present our mass reconstruction and estimation in Section 3. In Section 4, the WL masses are compared with the results from previous non-lensing studies before the summary is presented in Section 5.

Throughout the paper, we assume a flat ΛCDM cosmology with $\Omega_M = 1 - \Omega_\Lambda = 0.3$ and $h = 0.7$ to interpret the WL signal. We use the AB magnitude system corrected for the Milky Way foreground extinction, and quoted uncertainties are at the 1σ ($\sim$68.3%) level. We represent the cluster mass by M_{Δ_c}, the mass enclosed within a spherical radius inside which the mean density equals Δ_c times the critical density of the Universe at the cluster redshift.

2. HST Observations and Weak-lensing Analysis

2.1. HST Observations

We employ three HST programs in our WL analysis: PROP 12927 (PI: A. Newman) and PROP 12990 (PI: A. Muzzin) for JKCS 041, and PROP 15267 (PI: R. Canning) for XLSSC 122. PROP 12927 provides grism spectroscopy and imaging data with two WFC3/IR filters, F105W and F160W. The WFC3/IR images from this program are centered on the X-ray peak of JKCS 041 (Figure 1). The total integration times are 2671 s and 4509 s for F105W and F160W, respectively. PROP 12990 targeted galaxies $\sim 1'$ northwest of JKCS 041 and took a shallow (integration time of 812 s) and single-band (F160W) image. The total field size of the F160W observation is $\sim$8.8 arcmin^2, while the F105W image covers $\sim$6.3 arcmin^2. PROP 15267 includes grism spectroscopy and WFC3/IR imaging with F105W and F140W. The F105W image is acquired in a single visit, with a total integration of 2612 s, covering an area of $\sim$4.7 arcmin^2 (Figure 2). The F140W image is slightly wider ($\sim$6.2 arcmin^2) and deeper (total integration of 5170 s).

Because of the difference in the coverage, there are regions without color information. Hereafter, we refer to the region where color information is available as "Region A" (a common area enclosed by the yellow line in the upper left panels of Figures 1 and 2). The area outside "Region A" is referred to as "Region B," where only the F140W filter (for XLSSC 122) or the F160W filter (for JKCS 041) is available.

We reduced the HST WFC3/IR data following the procedures outlined in M. J. Jee et al. (2017) and J. Kim et al. (2019, 2021). Briefly, we first aligned the individual pipeline-processed, calibrated, flat-fielded (`FLT`) exposures with respect to a reference frame by obtaining astrometric solutions based on common astronomical sources in the overlapping regions. Next, we used the MultiDrizzle software (A. M. Koekemoer et al. 2003) to remove cosmic rays and sky background and to combine all exposures. We chose the Gaussian kernel with a `pixfrac` parameter of 0.7 and an output pixel scale of $0''.05$ per pixel. As a sanity check, we repeated the data reduction using `TweakReg` and `AstroDrizzle` in the DrizzlePac package (S. Gonzaga et al. 2012) and confirmed that the outputs are virtually identical.

Following the data reduction process, we detected objects with SExtractor (E. Bertin & S. Arnouts 1996) in dual-image mode. We created the detection image by stacking all

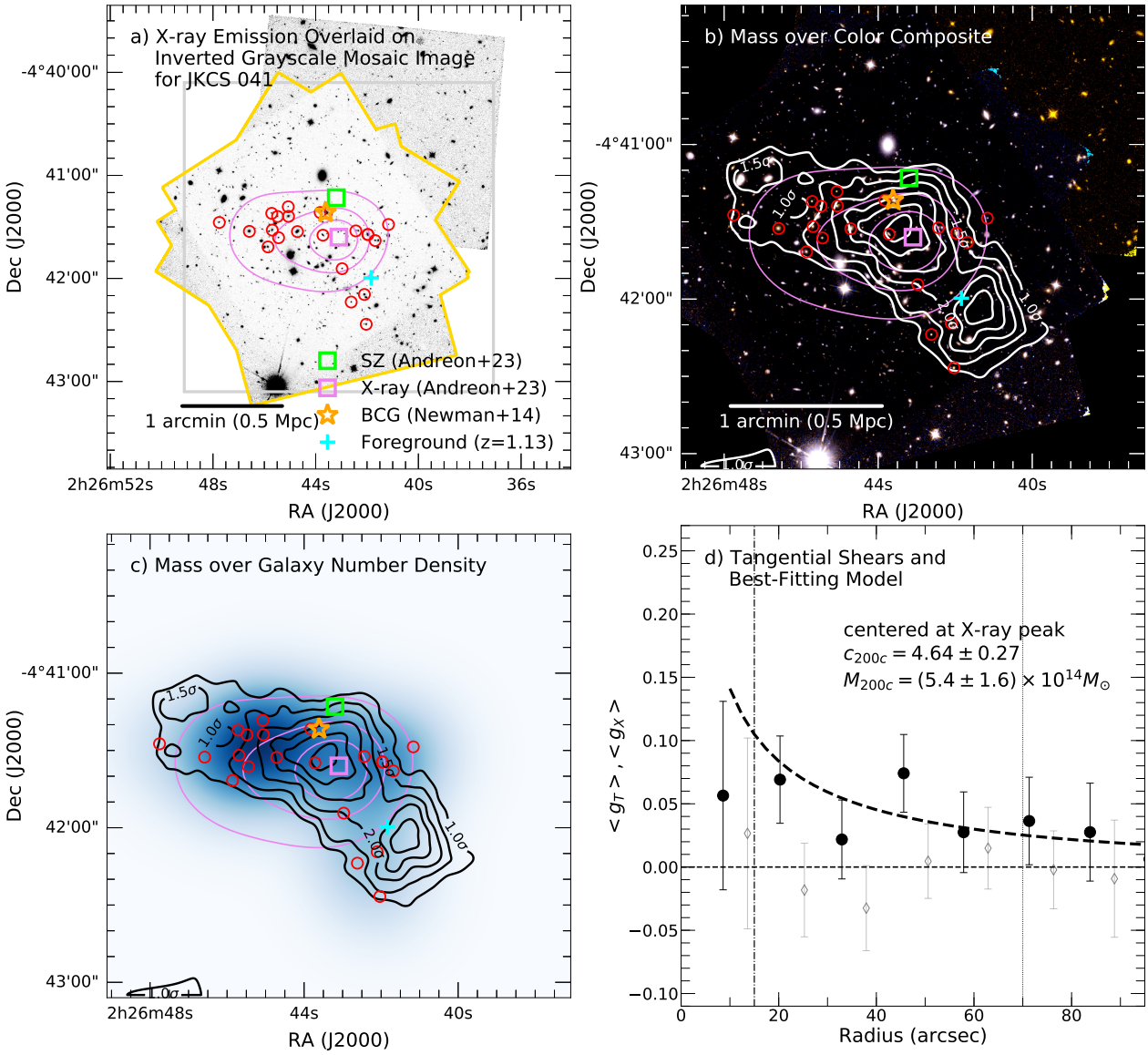

Figure 1. WL results of JKCS 041. Our two-dimensional (2D) mass reconstruction is obtained by FIATMAP. We denote the SZ peak with a green square, the X-ray peak with a violet square, the brightest cluster galaxy (BCG) position with an orange star, the foreground structure center at $z = 1.13$ with a cyan cross, and the spectroscopic members with red circles. (a) The footprint of the HST observation overlaid with X-ray emission contours (violet; S. Andreon et al. 2023). The inverted grayscale represents the intensity from the WFC3/IR F160W filter, while the yellow polygon outlines the footprint of the WFC3/IR F105W observation. The mass reconstruction is limited to the central $\sim 1.5 \times 1.5$ arcmin^2 region (gray box). (b) Mass (white) and X-ray emission (violet) contours overlaid on the color composite. This color composite is created using HST WFC3 IR/F105W (blue), the mean of WFC3 IR/F105W and WFC3 IR/F160W (green), and WFC3 IR/F160W (red). The outermost mass contour corresponds to 1σ significance, with significance increasing inward by 0.5σ, reaching a peak significance value of $\sim 3.7\sigma$. Our WL mass centroid is consistent with the X-ray peak. (c) Mass (black) and X-ray emission (violet) contours overlaid on the galaxy number density map of the confirmed cluster member galaxies from A. B. Newman et al. (2014). The smoothing scale of the number density map is FWHM $\sim 33''$. Overall, correlations are good between the galaxy number density map, the X-ray contours, and our WL mass contours. (d) Reduced tangential shear profile (filled circles) with respect to the X-ray peak. The cross shear profile (open diamonds), obtained by rotating the source galaxy images by 45°, is consistent with zero. The best-fit model under a single spherical NFW halo assumption with the mass–concentration relation of B. Diemer & M. Joyce (2019) is denoted with the dashed line. The dotted–dashed vertical line at $r \sim 15''$ indicates the cutoff radius inside which the signal is ignored in our NFW profile fitting. The dotted vertical line at $r \sim 70''$ marks the maximum radius where the azimuthal average can be obtained from a complete circle.

exposures according to their weights, and we identified objects if they have at least ten connected pixels above 1.5 times the sky rms.

2.2. Weak-lensing Analysis

2.2.1. Modeling Point-spread Function and Measuring Galaxy Shapes

The first step in our WL analysis is modeling the PSFs of source galaxies. Incorrect PSF modeling introduces additional distortion, thereby mimicking the WL signal. This systematic effect, resulting from PSF modeling errors, is particularly problematic for faint and small galaxies, comprising the majority of the source population in high-redshift galaxy cluster lensing. Following the methodology outlined in M. J. Jee et al. (2007), we generated PSF libraries for the WFC3/F140W and WFC3/F160W filters based on archival globular cluster field imaging data. These PSF libraries are then employed to identify the best-matching PSF template for each science exposure in the JKCS 041 and XLSSC 122 fields.

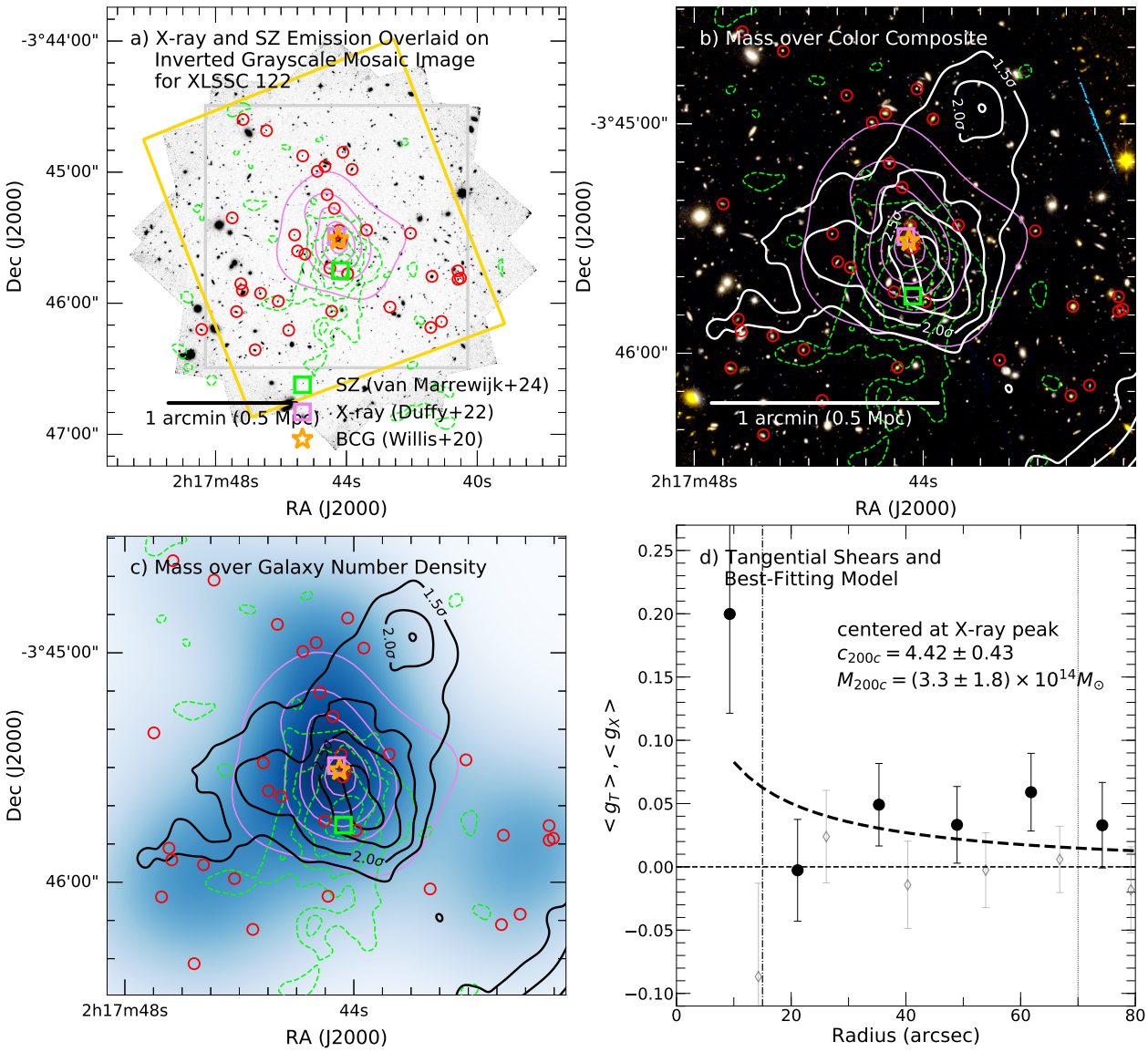

Figure 2. Same as Figure 1 but for XLSSC 122. (a) The footprint of the HST observation overlaid with X-ray (violet; J. van Marrewijk et al. 2024) and SZ (green; J. van Marrewijk et al. 2024) contours. The SZ peak, X-ray peak, and BCG position are indicated with a green square, a violet square, and an orange star, respectively. The inverted grayscale represents the intensity in F140W. The yellow box outlines the footprint of the F105W observation. Our WL mass reconstruction is performed on the central $\sim 1 \times 1$ arcmin^2 region marked by a gray box. (b) Mass (white), X-ray emission (violet), and SZ (green) contours overlaid on the color composite, which is created with F105W (blue), F105W+F140W (green), and F140W (red). The outermost mass contour corresponds to 1.5σ significance, with significance increasing inward by 0.5σ, reaching a peak significance value of $\sim 3.2\sigma$. Our WL mass centroid is consistent with the SZ, X-ray, and BCG centers. (c) Mass (black), X-ray emission (violet), and SZ (green) contours overlaid on a galaxy number density map created with the confirmed cluster member galaxies from J. P. Willis et al. (2020). (d) Reduced tangential shear profile with respect to the X-ray peak. The best-fit single spherical NFW model is indicated with the dashed line.

For detailed descriptions of the HST PSF modeling, readers are referred to M. J. Jee et al. (2007, 2017). We were unable to create a PSF library for the WFC3/F105W filter due to the limited number of suitable stellar fields in the archive.

We conducted the shape measurement of each object by fitting a two-dimensional (2D) elliptical Gaussian profile using the `MPFIT` (C. B. Markwardt 2009) package. Before the fitting, the 2D elliptical Gaussian model is convolved with the PSF model at each source position. The shape parameters of the model (e.g., orientation angle ϕ, semimajor axis a, and semiminor axis b) are utilized to determine the ellipticity $e = (a - b)/(a + b)$. We refer readers to J. Kim et al. (2019, 2021) for a detailed procedure of shape measurement.

In principle, the average ellipticity of the sources corresponds to the reduced shear g defined by $g = \gamma/(1 - \kappa)$, where κ is convergence and γ is shear (see a review by M. Bartelmann & P. Schneider 2001). However, the reduced shear does not exactly equal the averaged ellipticity due to systematic effects, including model bias and noise bias (e.g., A. Refregier et al. 2012; R. Massey et al. 2013). Here, we adopted a multiplicative correction factor of 1.25 determined by M. J. Jee et al. (2017). This value combines the shear multiplicative correction factor for the HST Advanced Camera for Surveys with an additional correction for undersampling bias in WFC3/IR. For further details, we refer the reader to M. J. Jee et al. (2017) and J. Kim et al. (2019).

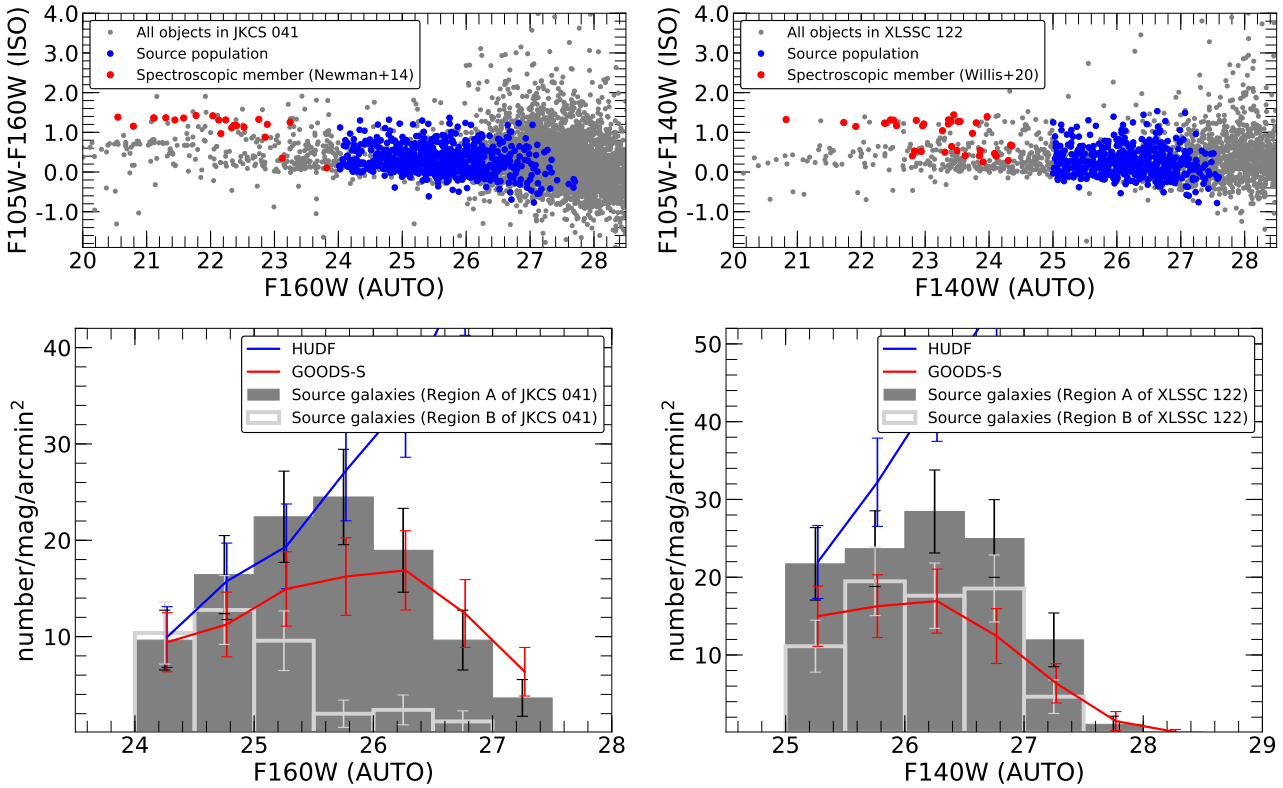

Figure 3. Color–magnitude relation and magnitude comparison with control fields for JKCS 041 and XLSSC 122. Top: color–magnitude relation for JKCS 041 (left) and XLSSC 122 (right). The cluster members are indicated in red. Both clusters exhibit a well-defined locus of the red sequence. Bottom: comparison of magnitude distributions between the source population in the cluster fields and those in the control fields. Error bars are computed based on Poissonian statistics. Given the good consistency between our source galaxies and those in the control fields in Region A, the contamination from possible members is insignificant. The rapid drop in the source magnitude distribution in Region B is due to the shallow depth.

2.2.2. Source Selection and Redshift Estimation

We selected the background source population that satisfies both the shape and photometric conditions and estimated their redshift distributions utilizing control fields, following the description in J. Kim et al. (2019, 2021). Here, we briefly explain the procedure.

The source selection starts with identifying objects with stable fitting status (`MPFIT STATUS`=1; C. B. Markwardt 2009) in shape measurement. We then removed too-small and too-faint objects, with ellipticity errors larger than 0.25 and semiminor axes smaller than 0.4 pixels. The remaining point-like sources are further excluded by discarding sources whose half-light radii are smaller than those of stars. Finally, residual spurious objects (e.g., diffraction spikes around bright stars, fragmented parts of foreground galaxies, clipped objects at the field boundaries, etc.) were manually identified and discarded.

After applying the shape requirements, we imposed photometric conditions in Region A, where color information is available: $24 < \mathrm{F160W} < 28$ with $\mathrm{F105W} - \mathrm{F160W} < 1.4$ and $25 < \mathrm{F140W} < 28$ with $\mathrm{F105W} - \mathrm{F140W} < 1.6$ for JKCS 041 and XLSSC 122, respectively. These criteria enable us to remove the cluster bright red-sequence galaxies (top panels of Figure 3). We also excluded the spectroscopic members using the publicly available catalogs from the literature (e.g., A. B. Newman et al. 2014; L. J. Prichard et al. 2017; J. P. Willis et al. 2020). For objects without color information (in Region B), only magnitude conditions $24 < \mathrm{F160W} < 28$ and $25 < \mathrm{F140W} < 28$ for JKCS 041 and XLSSC 122, respectively, were applied.

We examined possible residual contamination from blue cluster members and faint red-sequence galaxies in our source selection because we only removed spectroscopically confirmed blue members. We compared our source magnitude distributions with those of the two control fields: the Hubble Ultra Deep Field (HUDF; M. Rafelski et al. 2015) and the Great Observatories Origins Deep Survey (M. Giavalisco et al. 2004) after applying the same photometric conditions. The bottom panels of Figure 3 show that our source magnitude distribution in both clusters does not show any significant excess with respect to the ones from the HUDF at $\mathrm{F160W} < 26$ or $\mathrm{F140W} < 25.5$, which implies that the member contamination is negligible. The rapid drop of source number density at $\mathrm{F160W} > 26$ and $\mathrm{F140W} > 27$ stems from the fact that our observations are shallower than the HUDF; the 5σ limiting magnitudes are 27.4 and 28.8 for Region A in JKCS 041 and the HUDF, respectively. The source number densities in Region B are smaller than those in Region A and drop quickly because the region is shallower; the 5σ limiting magnitude is 26.4 in JKCS 041.

From the source selection described above, 766 galaxies, corresponding to a number density of $\sim 87\,\mathrm{arcmin}^{-2}$, are selected for JKCS 041. Due to the difference in the observation depth, the source density is higher in Region A with $\sim 106\,\mathrm{arcmin}^{-2}$ and $\sim 38\,\mathrm{arcmin}^{-2}$ for Regions A and B, respectively. In the XLSSC 122 field, 592 galaxies

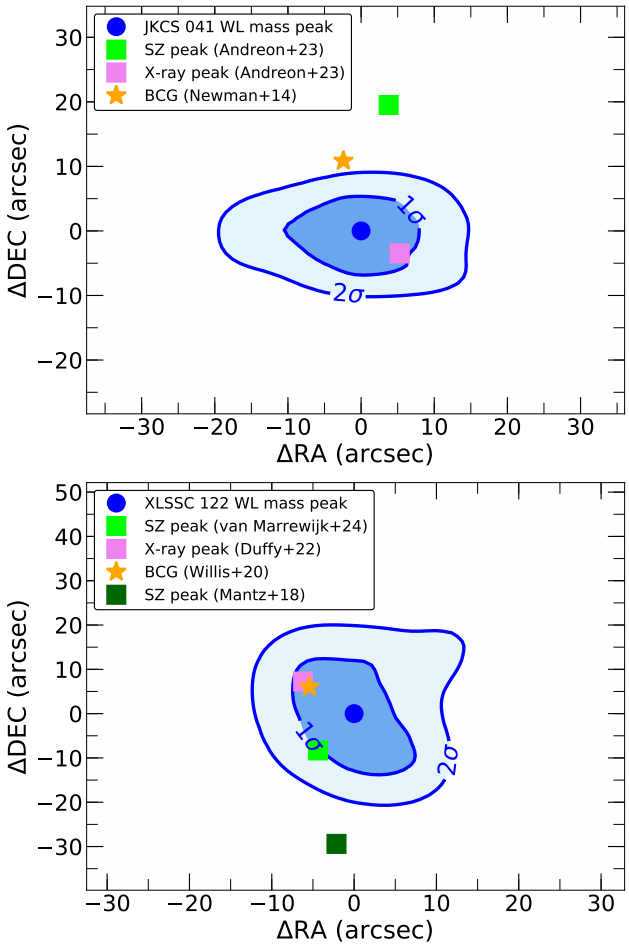

Figure 4. WL mass centroid significance distributions for JKCS 041 (top) and XLSSC 122 (bottom), based on 1000 bootstrap realizations. The centroid distributions for each cluster are represented by blue contours. For JKCS 041, the X-ray peak is enclosed within the 1σ region, whereas the BCG lies slightly beyond the 2σ contour. The SZ peak is offset from the WL mass centroid at the $\sim 3\sigma$ level. For XLSSC 122, the BCG, X-ray peak, and the SZ peak reported by J. van Marrewijk et al. (2024) are all consistent with the WL mass centroid within the 1σ level. In contrast, the SZ peak reported by A. B. Mantz et al. (2018) exhibits an offset of $\sim 2.8\sigma$.

($\sim 104\,\mathrm{arcmin}^{-2}$) are selected with $\sim 112\,\mathrm{arcmin}^{-2}$ and $\sim 71\,\mathrm{arcmin}^{-2}$ for Regions A and B, respectively.

We estimated the lensing efficiency β of our source population by employing the HUDF photo-z catalog after applying the same source selection conditions. Following the procedure in J. Kim et al. (2019, 2021), we find that the average lensing efficiencies $\langle\beta\rangle$ of source galaxies are $\langle\beta\rangle = 0.079$ (corresponding to $z_{\rm eff} = 2.085$) and $\langle\beta\rangle = 0.100$ (corresponding to $z_{\rm eff} = 2.180$) for Regions A and B, respectively, in the JKCS 041 field. Moreover, we accounted for the width of the source distribution since the assumption that all sources are at the same redshift plane causes systematic errors. The width of the source population is estimated by squaring the lensing efficiency of each source and taking the average, yielding $\langle\beta^2\rangle = 0.019$ and 0.023 for Regions A and B, respectively. We used the lensing efficiency $\langle\beta\rangle$ and its width $\langle\beta^2\rangle$ to apply the first-order correction derived by C. Seitz & P. Schneider (1997). For the source population in XLSSC 122, the lensing efficiency, its width, and effective source redshift in Region A (Region B) are $\langle\beta\rangle = 0.063$ (0.094), $\langle\beta^2\rangle = 0.014$ (0.021), and $z_{\rm eff} = 2.234$ (2.384), respectively.

3. Results

3.1. Mass Reconstruction

We reconstruct the 2D projected mass distribution with the FIATMAP code, which implements the KS93 (N. Kaiser & G. Squires 1993) Fourier inversion in real space (P. Fischer & J. A. Tyson 1997). We refer readers to D. Wittman et al. (2023) for a brief explanation of the code. We verify that the result is highly consistent with the KS93 inversion result. To determine the noise level, significance, and centroid uncertainty in our mass map, we employ the bootstrapping resampling method. We first resample our source galaxies 1000 times, allowing for redundancy. For each resampling, the corresponding mass map is generated and saved. We then create an uncertainty (rms) map from the resulting 1000 mass maps. A signal-to-noise ratio map is obtained by dividing the mean mass map by the rms map. The mass peak centroid uncertainty is determined from the distributions of the mass peak positions measured from the 1000 realizations (Figure 4).

We display our mass reconstruction results for two clusters in Figures 1 and 2. In JKCS 041, the mass centroid is $\sim 7''$, $\sim 11''$, and $\sim 20''$ away from the X-ray peak, brightest cluster galaxy (BCG), and SZ peak, respectively. Based on the WL mass centroid significance contours in the top panel of Figure 4, the X-ray peak falls within the 1σ contour, while the BCG lies slightly outside the 2σ contour. The distance between the SZ peak and our WL mass peak corresponds to $\sim 3\sigma$ of our WL mass centroid uncertainty. Recently, S. Andreon et al. (2023) argued that the offset between the X-ray and SZ peaks is one of the indicators that JKCS 041 is undergoing a major merger event. In XLSSC 122, the mass centroid is $\sim 15''$, $\sim 13''$, and $\sim 7''$ offset from the X-ray peak, BCG, and SZ peak, respectively. According to the centroid distribution in the bottom panel of Figure 4, the WL mass peak is spatially consistent with all three reference positions within the 1σ range.[7]

The mass peak significances reach $\sim 3.7\sigma$ and $\sim 3.2\sigma$ for JKCS 041 and XLSSC 122, respectively. The east–west elongation in the JKCS 041 mass map somewhat resembles the distribution of the cluster galaxies and X-ray emission, while the north–south elongation in XLSSC 122 is also reminiscent of the distribution of the galaxy and gas components. However, given the noise level of the current WL data, it is difficult to draw definitive conclusions about these observed patterns.

Scrutiny of our mass maps suggests that there are some hints of substructures in both clusters. In JKCS 041, we identify a mass clump in the southwestern (SW) region with a peak significance of $\sim 3.3\sigma$, located $\sim 39''$ (~ 334 kpc) from the X-ray peak. This SW clump is close to the southwest galaxy groups mentioned by L. J. Prichard et al. (2017). In addition, A. B. Newman et al. (2014) reported the presence of a foreground structure at $z = 1.13$ near the SW mass clump (cyan cross in Figure 1). Hence, firm conclusions cannot be reached until deeper WL data become available. Nevertheless, we investigate whether the SW clump is associated with a structure at a significantly lower redshift. This test is carried out by changing our source selection criteria in such a way that the source population includes a large number of the JKCS 041

[7] The first SZ centroid measurement of the cluster by the CARMA data (A. B. Mantz et al. 2018) is located $\sim 24''$ (~ 210 kpc) south of the WL mass centroid, corresponding to $\sim 2.8\sigma$ distance.

members. If the mass substructure comes from a much lower ($z \ll 1.8$) redshift, the JKCS 041 member galaxies are legitimate background galaxies. When we select brighter source galaxies (e.g., $22 < \mathrm{F160W} < 26$), including the JKCS 041 red sequence, the SW clump nearly disappears, while the main clump becomes weaker but is still visible. Our test suggests that the SW substructure in our mass map may not be associated with the $z = 1.13$ structure mentioned by A. B. Newman et al. (2014). In XLSSC 122, the NW mass peak $\sim 40''$ away from the main mass peak has a significance of $\sim 2.6\sigma$. It is difficult to associate this substructure with any galaxy overdensity.

3.2. Mass Estimation

We derive the mass of each cluster using a parametric approach, assuming that the mass profile of each cluster follows a single spherical Navarro–Frenk–White (NFW; J. F. Navarro et al. 1997) profile. The NFW profile has two free parameters: concentration (c) and mass (M). Since the two parameters are highly degenerate, mass measurements based on X-ray (e.g., S. Amodeo et al. 2016; R. T. Duffy et al. 2022) and WL analysis (e.g., H. Hoekstra et al. 2015; N. Martinet et al. 2016; M. J. Jee et al. 2017; H. Zohren et al. 2022) often assume a mass–concentration (M–c) relation to enable stable fitting. In this study, we adopt the mass–concentration (M–c) relation of B. Diemer & M. Joyce (2019; hereafter DJ19). However, it is worth mentioning that because both the NFW profile and the M–c relation describe average properties; the density profile of an individual cluster may significantly deviate from the average. We address the impact of this so-called model bias in Section 4.3.

Our χ^2 function is expressed as follows:

$$\chi^2 = \sum_i \sum_{j=1,2} \frac{[g_j^{\mathrm{model}} - g_j^{\mathrm{obs}}]^2}{\sigma_{\mathrm{SN}}^2 + \sigma_{e,i}^2}, \quad (1)$$

where

$$g_j^{\mathrm{model}} = g_j^{\mathrm{model}}(x_i, y_i, z_s, M, c, x_c, y_c), \quad (2)$$

and $g_j^{\mathrm{obs}} = g_j^{\mathrm{obs}}(x_i, y_i)$ are the jth components of the predicted and observed reduced shears of the ith source, respectively, at the position (x_i, y_i) at the source redshift z_s, given the cluster mass M centered at (x_c, y_c) with the concentration c. The quantities σ_{SN} and $\sigma_{e,i}$ are the ellipticity dispersion (shape noise) and measurement uncertainty, respectively. We set σ_{SN} to 0.25. The predicted reduced shear g^{model} follows a spherical NFW profile and the DJ19 M–c relation. We fit our model to the shapes of individual sources without binning by minimizing the χ^2 function in Equation (1). We choose the X-ray peak of each cluster as the fiducial centroid for mass measurement. The WL signal within $r < 15''$ is discarded to minimize a number of issues, including cluster member contamination, centroid uncertainty, nonlinearity, etc.

The bottom right panels of Figures 1 and 2 show the observed tangential shear profiles and the best-fit NFW model prediction. The resulting masses of JKCS 041 and XLSSC 122 are $M_{200c} = (5.4 \pm 1.6) \times 10^{14}\, M_\odot$ [$M_{500c} = (3.8 \pm 1.1 \times 10^{14}\, M_\odot$] and $M_{200c} = (3.3 \pm 1.8) \times 10^{14}\, M_\odot$ [$M_{500c} = (2.3 \pm 1.3) \times 10^{14}\, M_\odot$], respectively. The M_{500c} value is obtained by interpolating from the M_{200c} value, assuming the NFW profile with the DJ19 M–c relation.

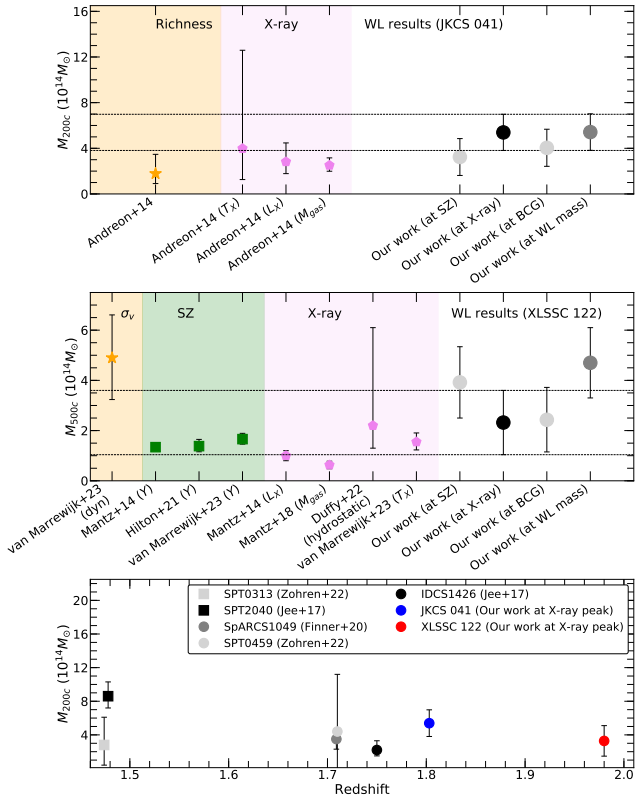

Figure 5. Mass comparison of JKCS 041 (top) and XLSSC 122 (middle) with various proxies and other high-z ($z \gtrsim 1.5$) clusters with WL mass measurements reported (bottom). For our WL mass representation, we adopt the best-fit NFW results with the DJ19 M–c relation under a single spherical halo assumption centered at the SZ, X-ray, BCG, and our WL mass centroid. Our WL mass results for both clusters are statistically consistent with previous mass estimates derived from member galaxies and gas components within the 1σ uncertainties. Additionally, our sample clusters exhibit similar mass estimates to galaxy clusters at lower redshift (e.g., $z \sim 1.7$).

To address miscentering (e.g., H. Martel et al. 2014), we repeat the mass measurements at three additional centroids: the SZ peak, BCG position, and WL mass centroid. The resulting masses for different center choices are highly consistent with the results obtained using the X-ray peaks. Quantitative comparisons are presented in Section 4.1.

4. Discussion

4.1. Mass Comparison

We compare previous mass estimates with our WL masses for JKCS 041 and XLSSC 122 in the top and middle panels of Figure 5, respectively. Note that as only M_{500c} values have been previously reported for XLSSC 122, we present our M_{500c} values in the middle panel.

The previous mass measurement of JKCS 041 was performed by S. Andreon et al. (2014), who determined the cluster's mass using four different mass proxies: richness, X-ray temperature, X-ray luminosity, and gas mass, based on mass–scaling relations. These proxies provided consistent mass estimates with $M_{200} > 10^{14.2}\, M_\odot$. S. Andreon et al. (2014) concluded the cluster is massive for its redshift ($z = 1.8$). The top panel of Figure 5 shows their results with 1σ uncertainties. Our WL mass estimates, with four different mass centroid choices, are consistent with them.

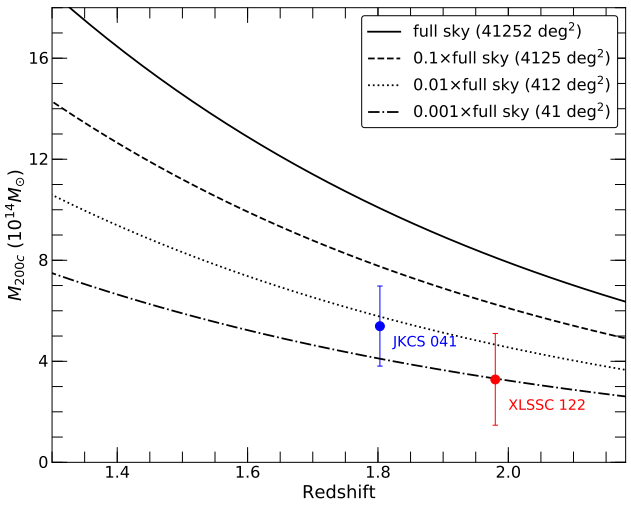

Figure 6. Exclusion curve and mass estimates of JKCS 041 and XLSSC 122. The exclusion curve considers sample and parameter variances within a 95% CL ($\sim 2\sigma$) for the full sky ($\sim$41,000 deg^2, solid), $\sim$4100 deg^2 (dashed), $\sim$410 deg^2 (dotted), and $\sim$41 deg^2 (dashed–dotted).

For XLSSC 122, several studies have measured the cluster mass using its member galaxies and intracluster medium. The X-ray and SZ mass estimates are within the range $M_{500c} = (1\text{–}2) \times 10^{14} M_\odot$ (A. B. Mantz et al. 2014, 2018; M. Hilton et al. 2021; J. van Marrewijk et al. 2024). Recently, J. van Marrewijk et al. (2024) suggested that the mass estimate based on velocity dispersion is $\sim$2.5 times greater than those derived from the hot gas. Our WL masses, measured with the X-ray and BCG centroids, are $M_{500c} \sim 2 \times 10^{14} M_\odot$, consistent with the gas-based mass estimates, while the 1σ error bars of our WL masses touch the 1σ lower limit of the dynamical mass. The WL masses obtained with the SZ and mass centroids are $M_{500c} = (4\text{–}5) \times 10^{14} M_\odot$, closer to the dynamical mass.

In the bottom panel of Figure 5, we compare our fiducial WL masses with five other high-redshift clusters at $z \gtrsim 1.5$: SPT-CL J0313-5334 ($z = 1.47$, SPT0313) and SPT0459 ($z = 1.71$) from H. Zohren et al. (2022), SPT-CL J2040-4451 ($z = 1.48$, SPT2040) and IDCS1426 ($z = 1.75$) from M. J. Jee et al. (2017), and SpARCS1049 ($z = 1.71$) from K. Finner et al. (2020). The most massive cluster at $z \gtrsim 1.5$ to date is SPT2040 at $z = 1.48$, whose mass is $M_{200} \sim 8 \times 10^{14} M_\odot$ (M. J. Jee et al. 2017). Apart from SPT2040, however, our two clusters, JKCS 041 and XLSSC 122, are comparable in mass to the other four clusters. Since the cluster mass function at its massive end decreases rapidly from $z = 1.5$ to $z = 2$, it is interesting to examine whether or not we can accommodate massive clusters such as JKCS 041 and XLSSC 122 at $z \sim 2$ within the current ΛCDM paradigm. We address this issue in Section 4.2.

4.2. Rarity

We study the rarity of JKCS 041 and XLSSC 122 using the exclusion curve test suggested by M. J. Mortonson et al. (2011). The exclusion curve represents the locus of the predicted maximum mass across redshift for a given cosmology and survey volume. It also accounts for parameter and sample variances of the cosmological model within a specified confidence level (CL). In Figure 6, we present exclusion curves at the 95% CL for both sample variance and parameter uncertainties for the areas of 41,000 deg^2 (full sky), 4100 deg^2, 410 deg^2, and 41 deg^2. A cluster with a mass and redshift above the curve for a given volume is unlikely to be observed within the corresponding survey under the ΛCDM model.

Our WL masses of the two clusters are comfortably below the exclusion curves for the 41,000 deg^2 and 4100 deg^2 surveys and overlap with the curves for the 410 deg^2 and 41 deg^2 surveys. It is important to note that our WL mass results shown here have not been corrected for Eddington bias, which arises from the steep mass function (A. S. Eddington 1913). Applying the Eddington bias correction (e.g., S. Andreon et al. 2009; M. J. Mortonson et al. 2011) would reduce the mass, increasing the compatibility of these two systems with ΛCDM cosmology.

4.3. Mass Systematics

In Section 3.2, we determine the masses of the two high-z clusters assuming the NFW halo profile with the DJ19 M–c relation. While WL is generally considered superior to other methods that require assumptions about hydrostatic equilibrium or scaling relations, it is important to note that WL mass estimation is subject to other systematics.

The M–c relation reflects the averaged properties of simulated galaxy clusters. Also, W. Lee et al. (2023) demonstrated that the mass and concentration of merging clusters vary depending on their merger phase. Additionally, the spherical NFW profile, an average representation from numerical simulations, does not account for the potentially inhomogeneous shapes of dark matter halos. Several studies (e.g., D. Clowe et al. 2004; M. Meneghetti et al. 2010; M. R. Becker & A. V. Kravtsov 2011; D. Gruen et al. 2015) have explored the mass uncertainties arising from deviations from spherical symmetry, such as halo triaxiality and orientation relative to the observer. High-z clusters like JKCS 041 and XLSSC 122, which are actively growing, may deviate from spherical symmetry and exhibit scatter in the M–c relation.

To examine the impact of model bias from the M–c relation and the assumption of a spherical NFW halo, we perform experiments using Markov Chain Monte Carlo (MCMC) analysis and aperture mass densitometry (AMD). The MCMC analysis allows us to probe the M–c parameter space freely without being constrained by a tight relation between the two parameters. If the resulting posteriors are significantly different from the result obtained with the M–c relation, this indicates that the systems may significantly deviate from the assumed relation. We employ flat priors for c_{200c} and M_{200c} with the intervals $1.5 < c_{200c} < 8$ and $10^{13} M_\odot < M_{200c} < 10^{16} M_\odot$, respectively. Figure 7 presents the posterior distributions for the mass and concentration parameters from 250,000 MCMC samples for JKCS 041 and XLSSC 122. The marginalized masses of JKCS 041 and XLSSC 122 are estimated to be $M_{200c} = 7.9^{+6.3}_{-3.2} \times 10^{14} M_\odot$ and $M_{200c} = 6.4^{+6.2}_{-3.3} \times 10^{14} M_\odot$, respectively. Although the median values are somewhat higher, the posteriors overlap with the results obtained with the M–c relation.

The AMD approach provides a projected mass profile without the need for a specific halo model. For a detailed description of this method, readers are referred to D. Clowe et al. (2000) and M. J. Jee et al. (2005). We find that the non-parametric AMD aperture mass aligns well with the parametric NFW aperture mass at R_{2500c}; because of the limited field size, the comparison is not feasible significantly beyond R_{2500c}, corresponding to $\sim 34''$ ($\sim$290 kpc) and $\sim 27''$ ($\sim$230 kpc) for

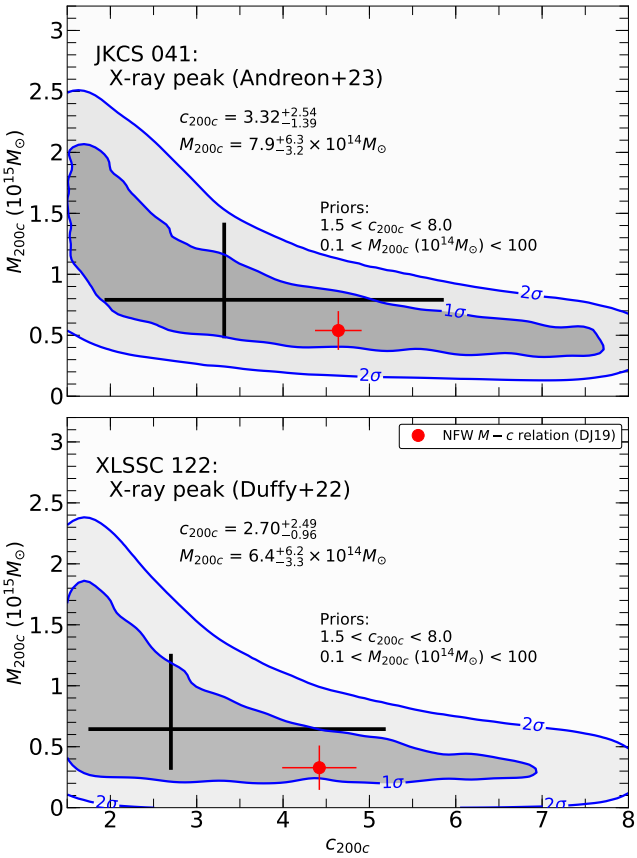

Figure 7. Posterior distributions based on 250,000 MCMC samples centered at the X-ray peaks for JKCS 041 (top) and XLSSC 122 (bottom), derived without assuming an M–c relation. The black crosses indicate the best-fit values and the associated uncertainties of c_{200c} and M_{200c}, obtained through one-dimensional marginalization. For comparison, the results obtained using the DJ19 M–c relation are also shown. The mass estimates from the MCMC samples are in good agreement with those derived using the DJ19 relation.

JKCS 041 and XLSSC 122, respectively. The 2D projected masses from the best-fit NFW models within the $r = R_{2500c}$ aperture are $M_{\mathrm{proj},2500c} = (2.5 \pm 0.5) \times 10^{14} M_\odot$ and $M_{\mathrm{proj},2500c} = (1.5 \pm 0.6) \times 10^{14} M_\odot$ for JKCS 041 and XLSSC 122, respectively. These values are consistent with the AMD aperture masses: $M_{\mathrm{proj},2500c} = (2.6 \pm 0.5) \times 10^{14} M_\odot$ and $M_{\mathrm{proj},2500c} = (2.0 \pm 0.4) \times 10^{14} M_\odot$ for JKCS 041 and XLSSC 122, respectively.

Finally, we consider large-scale structures along the line of sight that are uncorrelated with our high-z clusters. Following the H. Hoekstra (2003) recipe, we estimate that large-scale structures contribute to $\sigma_\gamma \sim 0.01$ within the angular scale that we probe (M. J. Jee et al. 2017), which corresponds to 15%–20% error in cluster mass estimation.

In summary, the above experiments indicate that the total error budgets in cluster mass are dominated by the statistical uncertainties for both clusters. However, given that the HST field is not sufficiently large enough to cover the virial radii of the clusters, it is necessary to revisit the issue with wider imaging data in a future study.

4.4. X-Ray–WL Mass Scaling Relation

WL mass serves as a calibrator for mass estimates derived from other mass proxies, such as X-ray and SZ observables. The relationship between mass and observables from gas

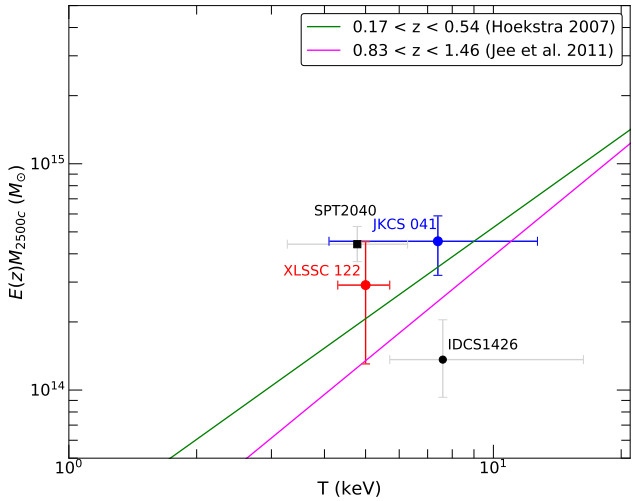

Figure 8. WL mass vs. X-ray temperature relation of our sample (JKCS 041 and XLSSC 122) and other high-z ($z \gtrsim 1.5$) clusters with X-ray and WL mass reported in the literature: WL masses from M. J. Jee et al. (2017) and X-ray temperatures from E. Bulbul et al. (2019) and M. Brodwin et al. (2016) for SPT2040 and IDCS1426, respectively. We display two best-fit results of the scaling relations at low-z ($M \propto T^{1.34}$; H. Hoekstra 2007) and high-z ($M \propto T^{1.54}$; M. J. Jee et al. 2011). JKCS 041 and XLSSC 122 follow the scaling relations measured from both low-z and high-z clusters.

components in galaxy clusters is typically characterized by a self-similar model (N. Kaiser 1986). While many studies have established WL mass-observable relations for low-redshift clusters (e.g., H. Hoekstra 2007; H. Hoekstra et al. 2015; S. L. Mulroy et al. 2019), far fewer have explored these relations at high redshifts (i.e., $0.8 < z < 1.7$; M. J. Jee et al. 2011; T. Schrabback et al. 2018, 2021; H. Zohren et al. 2022). Given that the two clusters in this study represent the most distant galaxy cluster sample where WL signals have been detected, we examine the locations of JKCS 041 and XLSSC 122 in the WL mass and X-ray temperature plane.

Figure 8 shows the locations of JKCS 041 and XLSSC 122 in the WL mass and X-ray temperature plane. We also display the relations for low- (H. Hoekstra 2007) and high-redshift (M. J. Jee et al. 2011) clusters from previous studies. For a consistent comparison with previous results, we convert our M_{200c} masses to M_{2500c}, assuming the NFW profile with the DJ19 M–c relation. We utilize the X-ray temperature measurements from S. Andreon et al. (2014) for JKCS 041 and from A. B. Mantz et al. (2018) for XLSSC 122. Together with JKCS 041 and XLSSC 122, we also include two other clusters at $z \gtrsim 1.5$, whose X-ray and WL mass measurements are available in the literature. JKCS 041 and XLSSC 122 follow the scaling relations of H. Hoekstra (2007) and M. J. Jee et al. (2011) well, while the other two clusters are marginally consistent with these scaling relations.

5. Summary

We present a WL study of the two high-redshift clusters JKCS 041 and XLSSC 122 at $z = 1.80$ and 1.98, respectively. They are the two most distant galaxy clusters to date ever measured with WL. Using the HST WFC3/IR imaging data and careful WL analysis, we successfully detected the WL mass peaks of JKCS 041 and XLSSC 122 at the $\sim 3.7\sigma$ and $\sim 3.2\sigma$ levels, respectively. The mass peak positions show good agreement with the X-ray peaks of the respective clusters.

Assuming a single spherical NFW halo following the DJ19 M–c relation centered on the X-ray peak, we determine the masses of JKCS 041 and XLSSC 122 to be $M_{200c} = (5.4 \pm 1.6) \times 10^{14}\,M_{\odot}$ and $M_{200c} = (3.3 \pm 1.8) \times 10^{14}\,M_{\odot}$, respectively. Our MCMC and AMD experiments suggest that the model bias due to the spherical NFW with the M–c relation may be subdominant with respect to the statistical uncertainty for both clusters.

Our exclusion curve test shows that although the two clusters are certainly extremely massive for their redshifts, their existence can comfortably be accommodated within the current ΛCDM paradigm. Finally, we conclude that JKCS 041 and XLSSC 122 well follow the mass–temperature scaling relations in the literature.

Acknowledgments

M.J.J. acknowledges support for the current research from the National Research Foundation (NRF) of Korea under the programs 2022R1A2C1003130 and RS-2023-00219959. J.K. and L.M. acknowledge support from the Beecroft Trust. We thank the anonymous referee for suggestions that improved the manuscript. This work is also based on observations made with the NASA/ESA Hubble Space Telescope (HST). The data presented in this paper were obtained from the Mikulski Archive for Space Telescopes (MAST) at the Space Telescope Science Institute. The specific observations analyzed can be accessed via doi:10.17909/tksy-qb78.

Software: MultiDrizzle (A. M. Koekemoer et al. 2003), DrizzlePac (S. Gonzaga et al. 2012), SExtractor (E. Bertin & S. Arnouts 1996), `MPFIT` (C. B. Markwardt 2009), `FIATMAP` (P. Fischer & J. A. Tyson 1997).

ORCID iDs

Jinhyub Kim https://orcid.org/0000-0003-2776-2761
M. James Jee https://orcid.org/0000-0002-5751-3697
Stefano Andreon https://orcid.org/0000-0002-2041-8784
Tony Mroczkowski https://orcid.org/0000-0003-3816-5372
Lance Miller https://orcid.org/0000-0002-3376-6200
Joshiwa van Marrewijk https://orcid.org/0000-0001-9830-3103
Hye Gyeong Khim https://orcid.org/0009-0006-5234-8406

References

Amodeo, S., Ettori, S., Capasso, R., et al. 2016, A&A, 590, A126
Andreon, S., Maughan, B., Trinchieri, G., et al. 2009, A&A, 507, 147
Andreon, S., Newman, A. B., Trinchieri, G., et al. 2014, A&A, 565, A120
Andreon, S., Romero, C., Aussel, H., et al. 2023, MNRAS, 522, 4301
Bahcall, N. A., & Fan, X. 1998, ApJ, 504, 1
Bahcall, N. A., Fan, X., & Cen, R. 1997, ApJL, 485, L53
Bartelmann, M., & Schneider, P. 2001, PhR, 340, 291
Becker, M. R., & Kravtsov, A. V. 2011, ApJ, 740, 25
Bertin, E., & Arnouts, S. 1996, A&AS, 117, 393
Bleem, L. E., Stalder, B., de Haan, T., et al. 2015, ApJS, 216, 27
Borgani, S., & Kravtsov, A. 2011, ASL, 4, 204
Brodwin, M., McDonald, M., Gonzalez, A. H., et al. 2016, ApJ, 817, 122
Bulbul, E., Chiu, I.-N., Mohr, J. J., et al. 2019, ApJ, 871, 50
Chiang, Y.-K., Overzier, R. A., Gebhardt, K., et al. 2017, ApJL, 844, L23
Clowe, D., De Lucia, G., & King, L. 2004, MNRAS, 350, 1038
Clowe, D., Luppino, G. A., Kaiser, N., & Gioia, I. M. 2000, ApJ, 539, 540
Diemer, B., & Joyce, M. 2019, ApJ, 871, 168
Duffy, R. T., Logan, C. H. A., Maughan, B. J., et al. 2022, MNRAS, 512, 2525
Dye, S., Warren, S. J., Hambly, N. C., et al. 2006, MNRAS, 372, 1227
Eddington, A. S. 1913, MNRAS, 73, 359
Fassbender, R., Böhringer, H., Nastasi, A., et al. 2011, NJPh, 13, 125014
Finner, K., James Jee, M., Webb, T., et al. 2020, ApJ, 893, 10
Fischer, P., & Tyson, J. A. 1997, AJ, 114, 14
Giavalisco, M., Ferguson, H. C., Koekemoer, A. M., et al. 2004, ApJL, 600, L93
Gonzaga, S., Hack, W., Fruchter, A., & Mack, J. 2012, The DrizzlePac Handbook (Baltimore, MD: STScI)
Gruen, D., Seitz, S., Becker, M. R., et al. 2015, MNRAS, 449, 4264
Hilton, M., Sifón, C., Madhavacheril, M., et al. 2021, ApJS, 253, 3
Hoekstra, H. 2003, MNRAS, 339, 1155
Hoekstra, H. 2007, MNRAS, 379, 317
Hoekstra, H., Herbonnet, R., Muzzin, A., et al. 2015, MNRAS, 449, 685
Jee, M. J., Blakeslee, J. P., Sirianni, M., et al. 2007, PASP, 119, 1403
Jee, M. J., Dawson, K. S., Hoekstra, H., et al. 2011, ApJ, 737, 59
Jee, M. J., Ko, J., Perlmutter, S., et al. 2017, ApJ, 847, 117
Jee, M. J., White, R. L., Benítez, N., et al. 2005, ApJ, 618, 46
Joo, H., & Jee, M. J. 2023, Natur, 613, 37
Kaiser, N. 1986, MNRAS, 222, 323
Kaiser, N., & Squires, G. 1993, ApJ, 404, 441
Kim, J., Jee, M. J., Hughes, J. P., et al. 2021, ApJ, 923, 101
Kim, J., Jee, M. J., Perlmutter, S., et al. 2019, ApJ, 887, 76
Koekemoer, A. M., Fruchter, A. S., Hook, R. N., & Hack, W. 2003, in The 2002 HST Calibration Workshop, Hubble after the Installation of the ACS and the NICMOS Cooling System, ed. S. Arribas, A. Koekemoer, & B. Whitmore (Baltimore, MD: STScI), 337
Lawrence, A., Warren, S. J., Almaini, O., et al. 2007, MNRAS, 379, 1599
Lee, W., Cha, S., Jee, M. J., et al. 2023, ApJ, 945, 71
Mantz, A. B., Abdulla, Z., Allen, S. W., et al. 2018, A&A, 620, A2
Mantz, A. B., Abdulla, Z., Carlstrom, J. E., et al. 2014, ApJ, 794, 157
Markwardt, C. B. 2009, in ASP Conf. Ser. 411, Astronomical Data Analysis Software and Systems XVIII, ed. D. A. Bohlender, D. Durand, & P. Dowler (San Francisco, CA: ASP), 251
Martel, H., Robichaud, F., & Barai, P. 2014, ApJ, 786, 79
Martinet, N., Clowe, D., Durret, F., et al. 2016, A&A, 590, A69
Massey, R., Hoekstra, H., Kitching, T., et al. 2013, MNRAS, 429, 661
Mehrtens, N., Romer, A. K., Hilton, M., et al. 2012, MNRAS, 423, 1024
Mei, S., Hatch, N. A., Amodeo, S., et al. 2023, A&A, 670, A58
Meneghetti, M., Rasia, E., Merten, J., et al. 2010, A&A, 514, A93
Mortonson, M. J., Hu, W., & Huterer, D. 2011, PhRvD, 83, 023015
Mulroy, S. L., Farahi, A., Evrard, A. E., et al. 2019, MNRAS, 484, 60
Navarro, J. F., Frenk, C. S., & White, S. D. M. 1997, ApJ, 490, 493
Nelson, K., Rudd, D. H., Shaw, L., et al. 2012, ApJ, 751, 121
Newman, A. B., Ellis, R. S., Andreon, S., et al. 2014, ApJ, 788, 51
Noordeh, E., Canning, R. E. A., Willis, J. P., et al. 2021, MNRAS, 507, 5272
Overzier, R. A. 2016, A&ARv, 24, 14
Pierre, M., Valtchanov, I., Altieri, B., et al. 2004, JCAP, 2004, 011
Planelles, S., Schleicher, D. R. G., & Bykov, A. M. 2015, SSRv, 188, 93
Prichard, L. J., Davies, R. L., Beifiori, A., et al. 2017, ApJ, 850, 203
Rafelski, M., Teplitz, H. I., Gardner, J. P., et al. 2015, AJ, 150, 31
Rasia, E., Lau, E. T., Borgani, S., et al. 2014, ApJ, 791, 96
Refregier, A., Kacprzak, T., Amara, A., et al. 2012, MNRAS, 425, 1951
Sartoris, B., Biviano, A., Fedeli, C., et al. 2016, MNRAS, 459, 1764
Schrabback, T., Applegate, D., Dietrich, J. P., et al. 2018, MNRAS, 474, 2635
Schrabback, T., Bocquet, S., Sommer, M., et al. 2021, MNRAS, 505, 3923
Seitz, C., & Schneider, P. 1997, A&A, 318, 687
van Marrewijk, J., Di Mascolo, L., Gill, A. S., et al. 2024, A&A, 689, A41
Wang, T., Elbaz, D., Daddi, E., et al. 2016, ApJ, 828, 56
Werner, S. V., Hatch, N. A., Matharu, J., et al. 2023, MNRAS, 523, 91
Willis, J. P., Canning, R. E. A., Noordeh, E. S., et al. 2020, Natur, 577, 39
Willis, J. P., Clerc, N., Bremer, M. N., et al. 2013, MNRAS, 430, 134
Wittman, D., Stancioli, R., Finner, K., et al. 2023, ApJ, 954, 36
Zohren, H., Schrabback, T., Bocquet, S., et al. 2022, A&A, 668, A18